Peer-reviewed version available at *Int. J. Environ. Res. Public Health* **2019**, *17*, 54; doi:10.3390/ijerph17010054

Simulation of Air Puff Tonometry Test Using Arbitrary Lagrangian-Eulerian (ALE) Deforming Mesh for Corneal Material Characterisation

Osama Maklad*[1]; Ashkan Eliasy[1]; Kai-Jung Chen[1]; Vassilios Theofilis[1]; Ahmed Elsheikh[1, 2, 3]

Affiliation:

[1] School of Engineering, University of Liverpool, Liverpool L69 3GH, UK
[2] NIHR Biomedical Research Centre for Ophthalmology, Moorfields Eye Hospital NHS Foundation Trust and UCL Institute of Ophthalmology, UK
[3] School of Biological Science and Biomedical Engineering, Beihang University, Beijing, China

***Corresponding author:**

Osama Maklad, School of Engineering, University of Liverpool, Brownlow Hill, Liverpool L69 3GH, UK, O.Maklad@liv.ac.uk, Tel: +44 (0) 748 143 2045

Data availability:

Data available from the Dryad Digital Repository:
https://datadryad.org/review?doi=doi:10.5061/dryad.cp5nt8v

Keywords: Ocular biomechanics; Intraocular pressure (IOP); Fluid Structure Interaction (FSI); Arbitrary Lagrangian-Eulerian mesh (ALE)

Abstract

Purpose: To improve numerical simulation of the non-contact tonometry test by using Arbitrary Eulerian-Lagrangian deforming mesh in the coupling between computational fluid dynamics model of an air jet and finite element model of the human eye.

Methods: Computational fluid dynamics model simulated impingement of the air puff and employed Spallart-Allmaras model to capture turbulence of the air jet. The time span of the jet was 30 ms and maximum Reynolds number $R_e = 2.3 \times 10^4$, with jet orifice diameter 2.4 mm and impinging distance 11 mm. Model of the human eye was analysed using finite element method with regional hyper-elastic material variation and patient specific topography for cornea and sclera starting from stress-free configuration. The cornea was free to deform as a response to the air puff using an adaptive deforming mesh at every time step of the solution. Aqueous and vitreous humours were simulated as a fluid cavity filled with incompressible fluid with a density of 1000 Kg/m3.

Results: Using the adaptive deforming mesh, in numerical simulation of the air puff test, improved the traditional understanding of how pressure distribution on cornea changes with time of the test. There was a mean decrease in maximum pressure (at corneal apex) of 6.29 ± 2.2% and a development of negative pressure on a peripheral corneal region 2-4 mm away from cornea centre.

Conclusions: The study presented an improvement of numerical simulation of the air puff test, which will lead to more accurate IOP and corneal material behaviour estimation. The parametric study showed that pressure of the air puff is different from model to another, value-wise and distribution-wise, based on cornea biomechanical parameters.

Peer-reviewed version available at Int. J. Environ. Res. Public Health 2019, 17, 54; doi:10.3390/ijerph17010054

1. Introduction

Biomechanical properties of biological tissues are important health indicators and multiple clinical decisions and surgical planning can be made based on their dynamic response to loading [1]. However, some of the mechanical and dynamic responses are still not fully understood due to the non-linearity and viscoelasticity of the tissues [2]. The tissue of interest in this study is the cornea , which contributes significantly to the optical focusing power of the eye and a vital area in refractive surgeries [3]–[5]. The air puff test conducted by the Ocular Response Analyser (ORA; Reichert, Inc., Buffalo, NY), the CorVis-ST (Oculus Optikgerate GmbH, Wetzlar, Germany) [6]–[8] and others, is a non-contact tonometry method with direct interaction with the cornea used to estimate intraocular pressure that is necessary for glaucoma management [9]–[11]. Moreover, this test was proven to have a promising potential in corneal material characterisation and Keratoconus detection [12]–[15].Tonometry is based on a simple concept of applying a known load causing deformation in the cornea and relating this load to the pressure inside the eye. However, accuracy of intraocular pressure (IOP) estimation continues to be a challenge due to the effect of corneal parameters including corneal geometry and material properties [16], [17]. The interplay between corneal geometry, material properties, ocular fluids and the air puff was studied before theoretically, numerically and clinically but with assumptions for the fluid structure interaction effect.

Theoretically, the air puff test was simulated as a harmonic oscillator model (1DOF) to model behaviour of the cornea under action of the air puff test by Zhaolong, Han et al. [18]. They investigated the air puff induced corneal vibrations and their effect on intraocular pressure (IOP), viscoelasticity and mass of the cornea based on theoretical approach and some clinical observations. Moreover, Anna Pandolfi et al. [19] used two different approaches to estimate intraocular pressure and the other eye parameters; the first approach was modelling the corneal system as a harmonic oscillator and in the second approach, they used patient specific geometries and finite element models to

Peer-reviewed version available at Int. J. Environ. Res. Public Health 2019, 17, 54; doi:10.3390/ijerph17010054

simulate the dynamic test on surgically treated corneas. The finite element calculations reproduced the observed clinical deformations of cornea including the two applanation configurations provided by Ocular Response Analyzer, suggesting that the mechanical response of cornea to the air puff test was driven only by elasticity of the stromal tissue. Furthermore, Kaneko et al. [20] modelled the human eyeball as a 1-DOF and 2-DOF systems to assess the dynamic response of the cornea and eyeball to the air puff test as shown in Figure 1.

Numerically, Kling et al. [21] presented a two-dimensional axis-symmetric finite element model which predicts deformation patterns of the cornea during air puff test to get its elastic and viscoelastic properties. They validated the results against experimental testing on porcine and human eyes to get the spatial pressure profile. They developed a 2D axis-symmetric CFD model for the air jet impinging on different solid configurations of the cornea. Their parametric study revealed significant contributions of intraocular pressure and corneal thickness to the corneal deformation, besides the corneal biomechanical properties [21]. Moreover, a patient specific finite element model of a healthy eye was presented by Ariza-Gracia et al. [22], taking account of the stress free configuration. The cornea was modelled as an anisotropic hyperelastic material with two preferential directions. Three sets of parameters within the healthy human range, based on inflation tests, were considered. A two-dimensional CFD simulation of the air jet was used to obtain pressure loading exerted on the anterior surface of the cornea, however, cornea was considered a solid non-deformable surface.

In another study performed by Muench et al. [23], they identified the normal and shear stress profiles on cornea resulting from an air puff to present a universal equation of the pressure distribution on cornea to use it for corneal material inverse analyses. Their method was based on experimental characterisation of the air puff produced by CorVis-ST and CFD simulation of the air puff test. As a calibration of the CFD simulations, they applied the air puff to a rigid eye model which was hung up through a yarn and positioned

Peer-reviewed version available at Int. J. Environ. Res. Public Health 2019, 17, 54; doi:10.3390/ijerph17010054

in front of the nozzle exit. They used eleven corneal deformation configurations to apply them in the CFD model, but also the cornea was simulated as a rigid surface. The outcomes showed dependency of pressure distribution on cornea on corneal deformations with minor effect of shear stress component on corneal deformations. In order to add a realistic modelling of the human eye, they considered the human face to see its influence on the pressure distribution on cornea. They demonstrated that pressure and shear stress distributions were not rotationally symmetric when applying the air puff to real human eyes [23].

Furthermore, using mesh-free particle method, Montanino et al. [24], [25] have proposed the first 3D fluid-solid interaction model between cornea and aqueous humour under the air puff test. Their numerical results confirmed the importance of including the internal fluids in simulation of the non-contact tonometry. However, they considered cornea only model and applied an analytical bell-shaped pressure distribution over the cornea with assumptions on the interaction between the air-puff and cornea. The closest fluid structure interaction simulation of the non-contact tonometry test was presented by Ariza-Garcia et al. [26], motivated by the fact that the proper interaction between the air and cornea is still unknown. They explored four different approaches starting from structural analysis to considering the fluid structure interaction with the air puff from outside and with the aqueous humour from inside. However, the model was created based on 2D-axisymmetric porcine eyes. The results indicated importance of considering fluid structure interaction effect on the pressure distribution and corneal deformations which will lead, if not considered, to an overestimated IOP measurements and biased corneal stiffness when performing the inverse finite element analysis [27]. To the best of our knowledge, the current study is the first attempt to quantify the influence of fluid structure interaction on corneal behaviour predictions for 3D patient specific eye models using the Arbitrary Lagrangian- Eulerian (ALE) deforming mesh, with more focus on air

Peer-reviewed version available at *Int. J. Environ. Res. Public Health* **2019**, *17*, 54; doi:10.3390/ijerph17010054

puff dynamics and extending the model for a larger parametric study aiming to develop IOP and corneal material estimation algorithms.

The impinging air puff is commonly studied assuming round jet diffusion and using impingement theory [28], [29]. In this theory, flow characteristics of impinging jets depend on parameters including jet orifice diameter, nozzle to impingement surface distance, jet confinement, radial distance from stagnation point, angle of impingement, surface curvature and roughness, nozzle exit geometry and turbulence intensity [30]–[32]. The round jet is characterized by a continuous increase in thickness of boundary shear layer. This boundary layer has two corresponding factors; a decrease in jet core cross-section and an increase in jet diameter, Figure 2(a). The core length depends on the inner angle of diffusion, about 5^{o} for the jet core and around 8.5^{o} for the outer jet diameter for highly turbulent impinging jets [33]. Figure 2(b) shows three regions of an impinging jet: the "free" jet region, the impingement or stagnation region, and the wall-jet region. In an earlier study, Larras considered the free and impinging jet regions and provided a detailed analysis of plane turbulent impinging jets [33].

The paper is arranged as follows; Section 2 states materials and numerical methods used in the analysis; Section 3 presents some of the achieved results; Section 4 provides a discussion about methods and results.

2. Materials and methods

Numerical model of the air puff test, shown in Figure 3, was constructed as a coupled model between computational fluid dynamics (CFD) and computational solid dynamics (CSD) as implemented in the software package ABAQUS (version 6.14, Dassault Systemes Simulia Inc., USA). The air puff test simulation consisted of three components:

- Three dimensional finite element model of the eye and material models for ocular tissues

Peer-reviewed version available at Int. J. Environ. Res. Public Health 2019, 17, 54; doi:10.3390/ijerph17010054

- Three dimensional CFD turbulence model of the air puff impinging on the cornea
- Fluid structure interaction (FSI) coupling between the two models

2. 1 Three dimensional eye model

The eye model consisted of 10,000 fifteen-nodded continuum elements (C3D15H), a general purpose element with 9 integration points, arranged over two layers, distributed along 15 rings in the cornea and 35 rings in the sclera. The corneal topography was based on the Pentacam measurements of topography and thickness profile. The Pentacam is a combined ocular device that employs a Scheimpflug camera and an illumination system which rotates around the eye to scan its topography [34]. The model also incorporated attributes to represent in-vivo conditions including the non-uniform thickness of cornea and sclera, weak inter-lamellar adhesion in corneal stroma and asphericity of the cornea's anterior and posterior surfaces [35].

The eye model included five different material definitions for cornea, limbus, anterior, equatorial and posterior sclera behaving hyper-elastically and their stiffness increases gradually under loading following an S-shaped stress-strain path as reported previously in experimental studies [36]–[38]. With these important features, the model was capable of selecting which stress-strain path (under loading or unloading) that each element would follow based on its strain history. The hyper-elastic materials have a rubber-like material behaviour and the strain energy potential function ($\prod$) is different than elastic materials and it takes multiple forms. The Ogden form was the one applied in the finite element model of the human eye [35], [39], [40].

$$\prod = \sum_{i=1}^{N} \frac{2\mu_i}{\alpha_i^2}(\bar{\lambda}_1^{\alpha_i} + \bar{\lambda}_2^{\alpha_i} + \bar{\lambda}_3^{\alpha_i} - 3) + \sum_{i=1}^{N} \frac{1}{D_i}(J^{el} - 1)^{2i} \quad (1)$$

where $\overline{\lambda_i}$ are the deviatoric principal stretches which are related to the deformations at constant volume as outcome of shear stresses; N defines order of the Ogden model with

Preprints (www.preprints.org) | NOT PEER-REVIEWED | Posted: 25 September 2019 doi:10.20944/preprints201909.0278.v1

Peer-reviewed version available at Int. J. Environ. Res. Public Health 2019, 17, 54; doi:10.3390/ijerph17010054

maximum of sixth order (N=6); μ and α are material parameters; J^{el} is the elastic volume ratio related to thermal expansion and D_i defines the material compressibility.

Finite element model of the eye was prevented from rigid body motion in the Z-direction (anterior-posterior) at the equatorial nodes. Also, the posterior and anterior pole nodes were restricted in X and Y directions, to prevent rotation, but were free to move in the Z-direction (anterior-posterior), see Figure 3, all the rest of nodes in the model were free to move in all directions. Before analysis, stress-free geometry of the eye was estimated. It is important to calculate the un-deformed configuration of the eye before applying the IOP, since deformed geometry of the eye will not be suitable for applying different values of IOP when performing the parametric study. An iterative approach was used to gradually move the mesh nodes to reach the stress-free (relaxed) configuration of the ocular tissue [35], [41]. An initial numerical model was generated based on a measured value of IOP and patient-specific geometry of the ocular tissue. The calculated deformations are then subtracted using inverse calculations from the stressed geometry to get the relaxed (stress-free) geometry.

In order to represent intraocular pressure inside the eye, the fluid cavity technique was used for this purpose. This technique was mainly used to simulate fluid-filled structures such as pressure vessels, hydraulic or pneumatic actuators and automotive air bags. The fluid cavity behaviour governs the relationship between cavity pressure, structure deformation and volume [38], [42], [43]. The fluid cavity calculates the change in IOP and internal volume during application of the air puff and corneal deformations. The fluid cavity was filled with a fluid with a density of (1,000 Kg/m^3) and bulk modulus of (2.2×10^3 MPa) [44]. A reference node was specified inside the cavity to represent the applied pressure and used in the volume calculations. Despite there are multiple components inside the eye including ocular lens, iris, aqueous and vitreous, the human eye was dealt with as a deformable pressure vessel that has internal pressure equal to IOP applied using a fluid cavity taking into account the change in pressure with the change in volume.

Peer-reviewed version available at *Int. J. Environ. Res. Public Health* **2019**, *17*, 54; doi:10.3390/ijerph17010054

2. 2 Three dimensional CFD turbulence model of the air puff

Model of the air puff consisted of 103,680 six-nodded 3-D fluid continuum elements (FC3D6) and used Spalart-Allmaras turbulent eddy viscosity model [45], [46] to simulate the turbulence in the air jet. The air model domain and mesh were created over the cornea and a 4 mm ring of the sclera by projecting coordinates of the anterior surface nodes to a distance of 11 mm from the cornea apex as shown in Figure 3. The projection principle was based on the concept of similar triangles to calculate new coordinates of the air domain as projected from the eye coordinates. It was important to generate a code which was applicable for all eye geometries, idealised and patient-specific, healthy or with certain pathological conditions. Material properties of air were defined in terms of density (1.204 Kg/m^3) and dynamic viscosity (1.83×10^{-5} Kg/(m.s)) [47], [48]. Amplitude of the air jet velocity, and its variation with time were defined according to Figure 4 based on experimental data obtained from the manufacturers of Corvis-ST (Corneal Visualization Scheimpflug Technology) and based on a simulated CFD model of the air flow inside the device starting from the piston to the nozzle [49]. The initial turbulent kinematic eddy viscosity was defined as four times the air kinematic viscosity (68×10^{-6} m^2/s) [42], [48]. The CFD solution parameters were then specified in terms of momentum, pressure and transport equation solvers and which turbulence model to be used to resolve the turbulent fluctuations. In the CFD model, the air jet inlet diameter was set to 2.4 mm, as measured for the nozzle of CorVis-ST, and the air maximum velocity at the inlet was set to 167.8 m/s. The surface that surrounds the jet diameter was set as a no-slip wall boundary condition and the side was open to the air with gauge pressure equal to zero. Lastly, the cornea and 4 mm ring from sclera, were set to a co-simulation, data exchange interface.

2. 3 Fluid-structure interaction co-simulation

In the fluid-structure coupled analysis, the eye finite element model imported the forces and lumped mass from the CFD model and exported deformations and velocities back

Peer-reviewed version available at Int. J. Environ. Res. Public Health 2019, 17, 54; doi:10.3390/ijerph17010054

to the CFD model at every time step (t_n) of the job as shown in Figure 5. The structure model calculates deformations (line 1) and sends them to the fluid model (line 2) which in turn calculates pressure loads (line 3) and returns them back to the structure model (line 4). For the co-simulation step to run successfully, the interaction surfaces in the eye and air models should be exactly the same with the same node numbering. The air puff test is a transient problem, and Abaqus/CFD used an advanced second-order projection method to create an arbitrary deforming mesh [50]. It used node-centred finite-element discretization for the pressure and a cell-centred finite volume discretisation of all other transported variables (such as velocity, temperature, turbulence, etc.) [42]. This hybrid meshing approach removed the need for any artificial dissipation, while preserving the traditional conservation properties associated with the finite volume method. The parallel preconditioned Krylov solvers (DSGMRES-ILUFGMRES) [51]–[53] were the main solution methods for transport equations including momentum and turbulence with prescribed iteration limit and convergence criteria, see Appendix 1. The pressure and distance function equations were solved with one of Krylov solvers and strong multigrid algebraic preconditioner such as (AMG-SSORCG-DSCG) [50], [54], [55].

The time was integrated using second-order accuracy and all other diffusive and advective terms were integrated using the Crank-Nicolson method [56]. The CFL (Courant-Friedrichs-Lewy) stability condition was satisfied also by continually adjusting the time increment size. The maximum value for CFL number was kept at 0.45. The CFL condition was necessary for partial differential equations' solution convergence [57], [58]. It must be less than one for explicit solvers to converge since the full numerical domain of dependence must contain the physical domain of dependence like Laney's definition [59].

2. 3.1 Arbitrary Lagrangian-Eulerian (ALE) deforming mesh

In FSI applications, where there are large solid deformations, the adaptive mesh is important for stability of the solution and to prevent distortion of the fluid mesh [60]–[62].

Peer-reviewed version available at Int. J. Environ. Res. Public Health 2019, 17, 54; doi:10.3390/ijerph17010054

That was done in the current model using Arbitrary Lagrangian-Eulerian (ALE) deforming mesh method which has the following characteristics; the mesh motion is constrained only at the free boundaries but everywhere else the material and mesh motion are independent. The adaptive meshing incorporates two main tasks; creating a new mesh and remapping the solution variables, through a process named advection, from the old mesh to the new mesh [60]–[63]. The meshing was created at a pre-specified frequency accompanied by a combination of mesh smoothing methods [42]. Then, remapping the solution variables to the new mesh is of second-order accuracy and conserves mass and momentum. Moreover, for FSI stabilisation, the solution control parameters were used to maintain mesh quality and control the mesh motion, see Appendix 1. The adaptive deformable mesh for a quarter model of the air puff model is shown in Figure 6 showing the initial mesh and the mesh at corneal highest concavity.

2. 4 Clinical dataset

A clinical dataset of 476 healthy patients from the Vincieye Clinic in Milan, Italy and Rio de Janeiro Corneal Tomography and Biomechanics Study Group, Brazil, was used to validate the numerical model. Institutional review board (IRB) ruled that approval was not obligatory for this record review study. However, the ethical standards as set in the 1964 Declaration of Helsinki, and revised in 2000, were observed. All patients provided informed consent before using their data in the study. All patients had a complete ophthalmic examination, including the CorVis ST and Pentacam (OCULUS Optikgeräte GmbH; Wetzlar, Germany) exams.

The inclusion criteria of healthy subjects were a Belin/Ambrósio Enhanced Ectasia total deviation index (BAD-D) of less than 1.6 the standard deviation (SD) from normative values in both eyes, no previous ocular surgery and disease, myopia less than 10D and no concurrent or previous glaucoma or hypotonic therapies [64]. Moreover, to confirm the diagnosis, all exams of each clinic were blindly re-evaluated by a corneal expert at the other clinic.

Peer-reviewed version available at Int. J. Environ. Res. Public Health 2019, 17, 54; doi:10.3390/ijerph17010054

Cornea biomechanical response parameters were collected from the CorVis-ST including maximum deformation, applanation pressures and times, highest concavity, spatial and temporal deformations with age ranging from (10-87 years), central corneal thickness (455-630 μm) and IOP (9-25 mmHg). Table 1 provides descriptive statistics of the clinical dataset for Milan and Rio's centres.

Patient specific numerical eye models were produced using an in house MATLAB code to perform a parametric study with wide range of CCT, IOP and corneal material properties starting from the stress-free geometry. Their deformation patterns, as a response to the air puff, were analysed and compared against the clinical behaviour.

3. Results

3. 1 Air puff traverses

The air puff was analysed to see change of the velocity, pressure and mesh deformation during the test. Figure 7 shows two velocity components of the air puff, the axial velocity (V3) normal to the cornea and velocity component (V1) parallel to the cornea at three normal traverses (Y/D=0, Y/D=1, Y/D=2), shown in Figure 3, and 4 time steps (T= 5, 8, 10, 16 ms). By the time, the puff gets stronger to reach its maximum strength at T= 16 ms and as the distance from the puff orifice increases, the normal velocity decreases until it reaches zero at the stagnation point on the cornea surface. By changing the path or the axial traverse further away from the cornea centre, the puff gets weaker and is noticed at (Y/D= 1 and 2), there are some negative values for the normal velocity indicating reflection of the air from cornea surface in the opposite direction to the flow. The jet accelerates parallel to the cornea forming a radial wall jet, developing with time and by going further from the cornea centre axis. This explains why there is a negative pressure observed at this location of the cornea. The pressure was found to change with corneal deformations and time steps as illustrated in Figure 8. It’s noticed from the plots that the distance from the jet at the end of every curve is increasing because of the

Peer-reviewed version available at Int. J. Environ. Res. Public Health 2019, 17, 54; doi:10.3390/ijerph17010054

movement of cornea with time of the test. Pressure here represents the static pressure, it starts with zero at the jet orifice and increase gradually towards the cornea because of transforming the dynamic pressure into static pressure.

Fluid structure interaction was found to have an effect on the pressure distribution on cornea during time of the air puff test. Figure 8(a) shows the pressure distribution change with time and the region where there is negative pressure. Graph (b) shows the progression of corneal deformation with time, while graph (c) indicates the difference between, taking the FSI effect into account, and ignoring it, through considering the cornea as a rigid, non-deformable, surface. Two different simulations of the turbulent jet were performed; one impinging on a rigid corneal surface with no moving boundaries and the other using FSI coupling between air and eye models to consider corneal deformations.

3. 2 Parametric study results

A parametric study was done on the coupled model of the air puff test by changing four parameters of the eye model and simulating response of the cornea to the air puff, this gives a great understanding of how corneal biomechanical parameters affect its deformation, which in turn, affect IOP measurement and corneal material estimation. The four parameters involved in the study were:

- Cornea material stiffness coefficient (μ)
- Central corneal thickness (CCT)
- Corneal curvature radius (R)
- Intraocular pressure (IOP)

The total number of models included in the study were 110 models with wide ranges for CCT, IOP, R and corneal material coefficient (μ) representing the change in corneal stiffness. Figure 9 shows the influence matrix of IOP and corneal material on dynamic

Peer-reviewed version available at Int. J. Environ. Res. Public Health 2019, 17, 54; doi:10.3390/ijerph17010054

corneal response parameters with different colour for each value. In graph (a) six corneal response parameters were plotted against each other and at different levels of IOP. The first row for the highest concavity (HC) deformation, is the most explaining parameter. By increasing IOP, the HC deformation is lower. The opposite is happening with the stiffness parameter (SP-HC), equation (2), for higher IOP, the stiffness parameter is higher. In graph (b), by increasing the stiffness of corneal material, the amount of deformation decreases and the peak distance (PD) between the applanation points shows the same trend. Graph (c) illustrates the corneal profile stages from initial geometry to highest concavity.

$$\text{SP-HC} = \frac{\text{AP1} - \text{IOP}}{\text{HC deformation} - \text{A1 deformation}} \qquad (2)$$

After showing, graphically, influence of the parameters involved in the parametric study, it was vital to quantify correlations and significance of relationships between parametric study's input and output parameters, to choose which response parameters were influenced more by changing IOP and corneal stiffness. This was an important outcome of the present study, as estimation algorithms for IOP and corneal material behaviour are required to correct fluid structure interaction effect between the air puff and human cornea. A bivariate correlation analysis using SPSS statistics (version 24, IBM Corp.) was performed to obtain Pearson's correlation coefficient (r) and two-tailed significance t-test to know the significance level of correlations (P-value). Descriptive statistics of the parametric study are shown in Table 2 providing mean, standard deviation, minimum and maximum of input and output parameters for 110 different eye models.

Table 3 provides values of Pearson's correlation coefficient (r) between input and output response parameters which gives an indication on correlation's strength and direction. The highest correlated parameters to IOP change were; first applanation pressure (AP1), first applanation velocity (A1 velocity), first applanation time (A1 time) with r= 0.736, .731, .725, respectively, and all of them at significance level of 0.0001 ($P < 0.0001$) referenced

Peer-reviewed version available at Int. J. Environ. Res. Public Health 2019, 17, 54; doi:10.3390/ijerph17010054

by the double asterisk next to the value of r. One of these three corneal response parameters was chosen, along with central corneal thickness (CCT), corneal curvature (R) and corneal material stiffness parameter (μ), to enter an estimation algorithm for IOP. On the other hand, the first applanation length (A1 length) and stiffness parameter (SP-HC) were the most associated response parameters to corneal material change with correlation coefficients of 0.471 and 0.442 respectively at significance level of 0.01 ($P < 0.01$).

3. 3 Clinical validation of numerical results

A set of clinical data for 476 patients from Milan and Rio datasets were used in the validation process. All patients have performed the air puff test using the same device (CorVis-ST). The spatial and temporal corneal deformations for three patients are shown in Figure 10 in comparison with the deformations from patient specific fluid-structure interaction models. A good agreement and close behaviour to the clinical corneal behaviour was achieved. The left column of graphs shows the spatial corneal deformation profiles at four time steps T= 5, 8, 10, 16 ms. The difference in profiles is due to the fact that biological tissue is different in responding to the air puff and is not guaranteed that the puff is applied to the cornea centre with the same angle and distance from the nozzle. The right column of figures shows the temporal apical deformation numerically and clinically with the value of root mean square error shown on the top.

In order to validate the parametric study, the same descriptive statistics and correlation analysis, which were done for the parametric study, were performed to the clinical dataset to see if there are any differences, before considering them in the IOP estimation algorithm in the future. Figure 11, provides a bar-chart to compare the means and standard deviations of the dynamic corneal response parameters numerically and clinically. The biggest difference was in the first applanation deformation amplitude with 76.9 % higher and HC deformation amplitude with 22.2 % less. In terms of Pearson's correlations, the clinical dataset showed that the first applanation pressure remained the

Peer-reviewed version available at Int. J. Environ. Res. Public Health 2019, 17, 54; doi:10.3390/ijerph17010054

highest correlated parameter to IOP (r=.927, P<.0001) followed by A1 time (r=.889, P<.0001) and stiffness parameter (SP-HC) (r=.857, P<.0001) which is the same as the numerical database apart from A1 velocity which was found the highest after AP1.

4. Discussion

The current study made use of numerical simulation of the non-contact tonometry test and the parametric study to better understand the corneal material behaviour under dynamic loading with more focus on the fluid structure interaction from outside the eye. The accurate material characterisation for cornea can help ophthalmologists and surgeons in treatment management and surgical planning before any physical intervention. Understanding the material mechanical response can be used in diagnosis of some diseases which alter the corneal stiffness such as keratoconus and ectatic diseases [65]–[67]. On the other hand, biomechanical correction of IOP measurement has been the focus of many studies in the past [14], [49], [68]. Some studies focused on the association of IOP with central corneal thickness CCT and corneal curvature radius R, other studies studied the material properties effect, but most of the them were structural in nature with no sufficient consideration to the fluid structure interaction effect between cornea and the air puff.

In order to accurately take into account, fluid structure interaction effect on the corneal response to loading, the two domains need to be solved simultaneously to exchange the data between them at each time step of the solution. The finite element model of the eye was based on the mass, force and stiffness matrices to calculate the structural material deformation. On the other hand, the CFD model of the air jet was governed by momentum and continuity equations to calculate pressure and velocity fields of the flow.

The coupled model of fluid structure interaction (FSI) between the eye and an air puff was successfully built and validated through comparison of the corneal deformations from the numerical model against clinical corneal response parameters acquired from CorVis-ST for in-vivo human eyes. The clinical comparisons were presented in two

Peer-reviewed version available at Int. J. Environ. Res. Public Health 2019, 17, 54; doi:10.3390/ijerph17010054

forms; the first form was by presenting cornea deformation profiles at 4 time captures of the test (5, 8, 10, 16 ms) along with the temporal apical corneal deformation, which has shown close but not perfect agreement. This is due to the fact that soft tissue materials are not easily to be expected and represented numerically through one material model. The second form was through calculating dynamic corneal response (DCR) parameters (A1 Time (ms), A1 Length (mm), A1 Velocity (mm/s), HC Time (ms), Peak Distance (mm), A1 Deformation Amplitude (mm), HC Deformation Amplitude (mm), AP1 (mmHg), SP-HC Stiffness parameter) and comparing them against the same parameters obtained clinically. These correlation analysis produced between these parameters will be used in the near future to develop a new corneal material estimation algorithm which does not depend only on patient's age but also depends on the patient specific corneal response parameters.

The air puff was analysed for three main variables, the axial velocity (V3), the parallel velocity (V1) and the pressure (P). These three variables give indication on the validity of the solution in both models, the CFD and the FE. Values of V3 and V1 validated the near wall treatment of the CFD code, the transport equations' solution at the impingement region and wall jet region, which is more obvious at (Y/D=1, 2).

From the results, there are some limitations appeared when comparing between the numerical and the clinical deformations, this difference refers to more than one parameter. The first parameter is the boundary conditions applied to the eye model. The eye model was supported from the equatorial nodes to prevent movement in the (Anterior-posterior) direction. There is some work in progress to simulate the fatty tissue around the eye to remove that boundary condition and allow whole eye movement. Another important material effect is the hysteresis influence which is related to the viscoelastic behaviour of the cornea. When the cornea reflects back after the application of the air puff, it has some relaxation time and memory effect to return back to the original geometry. A third parameter is the air puff shooting direction which can be sometimes at

Peer-reviewed version available at Int. J. Environ. Res. Public Health 2019, 17, 54; doi:10.3390/ijerph17010054

an angle from the eye axis and a modification for the mesh was done to apply the air puff at an angle same as the clinical shooting.

Ethical statement

A clinical dataset of 476 healthy patients from the Vincieye Clinic in Milan, Italy and Rio de Janeiro Corneal Tomography and Biomechanics Study Group, Brazil, was used to validate the numerical model. Institutional review board (IRB) ruled that approval was not obligatory for this record review study. However, the ethical standards as set in the 1964 Declaration of Helsinki, and revised in 2000, were observed. All patients provided informed consent before using their data in the study. All patients had a complete ophthalmic examination, including the CorVis-ST and Pentacam (OCULUS Optikgeräte GmbH; Wetzlar, Germany) exams. The inclusion criteria of healthy subjects were a Belin/ Ambrósio Enhanced Ectasia total deviation index (BAD-D) of less than 1.6 the standard deviation (SD) from normative values in both eyes, no previous ocular surgery and disease, myopia less than 10D and no concurrent or previous glaucoma or hypotonic therapies [64]. Moreover, to confirm the diagnosis, all exams of each clinic were blindly re-evaluated by a corneal expert at the other clinic.

Conflict of interest statement

Prof. Elsheikh is a consultant for OCULUS Optikgeräte GmbH. None of the remaining authors have financial disclosures or personal interests in the work reported in this paper.

Funding statement

No funding received to support this research.

Acknowledgement

We would like to acknowledge the Vincieye Clinic in Milan, Italy and Rio de Janeiro Corneal Tomography and Biomechanics Study Group, Brazil for permission to work on

the clinical data provided. Great appreciation to OCULUS Optikgeräte GmbH for their support with CorVis-ST.

Nomenclature

IOP	Intraocular Pressure
CCT	Central Corneal Thickness
CFD	Computational Fluid Dynamics
FE	Finite Element
FSI	Fluid Structure Interaction
ALE	Arbitrary Lagrangian-Eulerian
$CorVis-ST$	Corneal Visualisation Scheimpflug Technology
ORA	Ocular Response Analyser
R_E	Reynolds number
HCR	Highest Concavity Radius
PD	Peak Distance
$SP-HC$	Stiffness Parameter at highest concavity
CDR	Corneal Deformation Response

Peer-reviewed version available at *Int. J. Environ. Res. Public Health* **2019**, *17*, 54; doi:10.3390/ijerph17010054

References

[1] *Fundamentals of Biomechanics*. Boston, MA: Springer US, 2007.

[2] J. Liu and C. J. Roberts, “Influence of corneal biomechanical properties on intraocular pressure measurement: Quantitative analysis,” *J. Cataract Refract. Surg.*, vol. 31, no. 1, pp. 146–155, 2005.

[3] P. Hanselaer, “The Human Eye,” *Nature*, vol. 10, no. 248, pp. 243–243, 1874.

[4] “Surgery for Refractive Errors,” *Lancet*, vol. 325, no. 8426, pp. 435–436, 1985.

[5] G. M. Cochrane, R. Du Toit, and R. T. Le Mesurier, “Management of refractive errors,” *BMJ (Online)*, vol. 340, no. 7751. pp. 855–860, 2010.

[6] D. Luce, “Air–Jet Temporal and Spatial Pressure Properties of the Reichert Ocular Response Analyzer (ORA),” *Invest. Ophthalmol. Vis. Sci.*, vol. 46, no. 13, pp. 5009–5009, May 2005.

[7] D. A. Luce, “Determining in vivo biomechanical properties of the cornea with an ocular response analyzer,” *J. Cataract Refract. Surg.*, vol. 31, no. 1, pp. 156–162, Jan. 2005.

[8] R. Ambrósio *et al.*, “Dynamic ultra high speed scheimpflug imaging for assessing corneal biomechanical properties,” *Rev. Bras. Oftalmol.*, vol. 72, no. 2, pp. 99–102, 2013.

[9] T.-H. Kwon, J. Ghaboussi, D. a Pecknold, and Y. Hashash, “Role of corneal biomechanical properties in applanation tonometry measurements.,” *J. Refract. Surg.*, vol. 26, no. 7, pp. 512–519, 2010.

[10] A. Elsheikh, C. W. McMonnies, C. Whitford, and G. C. Boneham, “In vivo study of corneal responses to increased intraocular pressure loading,” *Eye Vis.*, vol. 2,

no. 1, p. 20, 2015.

[11] O. Abitbol, J. Bouden, S. Doan, T. Hoang-Xuan, and D. Gatinel, “Corneal hysteresis measured with the ocular response analyzer®in normal and glaucomatous eyes,” *Acta Ophthalmol.*, vol. 88, no. 1, pp. 116–119, 2010.

[12] T. T. Andreassen, A. Hjorth Simonsen, and H. Oxlund, “Biomechanical properties of keratoconus and normal corneas,” *Exp. Eye Res.*, vol. 31, no. 4, pp. 435–441, 1980.

[13] R. Vinciguerra *et al.*, “Detection of Keratoconus With a New Biomechanical Index,” *J. Refract. Surg.*, vol. 32, no. 12, pp. 803–810, 2016.

[14] A. Eliasy *et al.*, “Ex-vivo experimental validation of biomechanically-corrected intraocular pressure measurements on human eyes using the CorVis ST,” *Exp. Eye Res.*, vol. 175, no. June, pp. 98–102, 2018.

[15] F. Bao, B. Geraghty, Q. Wang, and A. Elsheikh, “Consideration of corneal biomechanics in the diagnosis and management of keratoconus: is it important?,” *Eye Vis.*, vol. 3, no. 1, p. 18, Dec. 2016.

[16] D. P. Piñero and N. Alcón, “Corneal biomechanics: a review,” *Clin. Exp. Optom.*, vol. 98, no. 2, pp. 107–116, Mar. 2015.

[17] J. Kerautret, J. Colin, D. Touboul, and C. Roberts, “Biomechanical characteristics of the ectatic cornea,” *J. Cataract Refract. Surg.*, vol. 34, no. 3, pp. 510–513, 2008.

[18] Z. Han *et al.*, “Air Puff Induced Corneal Vibrations: Theoretical Simulations and Clinical Observations,” *J. Refract. Surg.*, vol. 30, no. 3, pp. 208–213, 2014.

[19] A. P. Irene Simoninia, Maurizio Angelillob, “Theoretical and numerical analysis of the corneal air pu ff test.”

[20] M. Kaneko, K. Tokuda, and T. Kawahara, “Dynamic sensing of human eye,” *IEEE Int. Conf. Robot. Autom.*, no. April, pp. 2871–2876, 2005.

[21] S. Kling, N. Bekesi, C. Dorronsoro, D. Pascual, and S. Marcos, “Corneal viscoelastic properties from finite-element analysis of in vivo air-puff deformation,” *PLoS One*, vol. 9, no. 8, 2014.

[22] M. Ariza-Gracia, J. F. Zurita, D. P. Piñero, J. F. Rodriguez-Matas, and B. Calvo, “Coupled biomechanical response of the cornea assessed by non-contact tonometry. A simulation study,” *PLoS One*, vol. 10, no. 3, pp. 1–15, 2015.

[23] S. Muench, · M Roellig, · E Spoerl, and · D Balzani, “Numerical and Experimental Study of the Spatial Stress Distribution on the Cornea Surface During a Non-Contact Tonometry Examination,” 2018.

[24] A. Montanino, M. Angelillo, and A. Pandolfi, “Modelling with a meshfree approach the cornea-aqueous humor interaction during the air puff test,” *J. Mech. Behav. Biomed. Mater.*, vol. 77, no. March 2017, pp. 205–216, 2018.

[25] A. Montanino, M. Angelillo, and A. Pandolfi, “A 3D fluid-solid interaction model of the air puff test in the human cornea,” *J. Mech. Behav. Biomed. Mater.*, vol. 94, pp. 22–31, Jun. 2019.

[26] M. Á. Ariza-Gracia, W. Wu, B. Calvo, M. Malvè, P. Büchler, and J. F. Rodriguez Matas, “Fluid–structure simulation of a general non-contact tonometry. A required complexity?,” *Comput. Methods Appl. Mech. Eng.*, vol. 340, pp. 202–215, Oct. 2018.

[27] B. A. Nguyen, C. J. Roberts, and M. A. Reilly, “Biomechanical Impact of the Sclera on Corneal Deformation Response to an Air-Puff: A Finite-Element Study,” *Front. Bioeng. Biotechnol.*, vol. 6, no. January, pp. 1–8, 2019.

[28] M. K. Looneytand, “Mean-flow and turbulent characteristics of free and impinging

jet flaws," *J. Fluid Mech*, vol. 147, pp. 397–429, 2018.

[29] T. J. Craft, L. J. W. Graham, and B. E. Launder, "Impinging jet studies for turbulence model assessment—II. An examination of the performance of four turbulence models," *Int. J. Heat Mass Transf.*, vol. 36, no. 10, pp. 2685–2697, Jul. 1993.

[30] J. W. Gauntner, J. N. B. Livingood, and P. Hrycak, "Survey of literature on flow characteristics of a single turbulent jet impinging on a flat plate," *NASA Tech. Memo.*, no. February, p. 43, 1970.

[31] C. Donaldson and R. Snedeker, "A study of free jet impingement. Part 1. Mean properties of free and impinging jets," *J. Fluid Mech*, vol. 45, no. 2, p. 281, 1971.

[32] K. J. Hammad and I. Milanovic, "Flow Structure in the Near-Wall Region of a Submerged Impinging Jet," *J. Fluids Eng.*, vol. 133, no. 9, p. 91205, 2011.

[33] J. Larras, "Plane turbulent impinging jets," *J. Hydraul. Res.*, vol. 12, no. 2, pp. 279–282, 1974.

[34] O. O. Gmbh, "Pentacam measurement principle," 2019. [Online]. Available: https://www.pentacam.com/int/technology/measurement-principle-licences-network.html. [Accessed: 27-Jan-2019].

[35] A. Elsheikh, C. Whitford, R. Hamarashid, W. Kassem, A. Joda, and P. Büchler, "Stress free configuration of the human eye," *Med. Eng. Phys.*, vol. 35, no. 2, pp. 211–216, Feb. 2013.

[36] A. Kotecha, A. Elsheikh, C. R. Roberts, H. Zhu, and D. F. Garway-Heath, "Corneal thickness- and age-related biomechanical properties of the cornea measured with the ocular response analyzer," *Investig. Ophthalmol. Vis. Sci.*, vol. 47, no. 12, pp. 5337–5347, 2006.

[37] A. Elsheikh, B. Geraghty, D. Alhasso, J. Knappett, M. Campanelli, and P. Rama,

"Regional variation in the biomechanical properties of the human sclera," *Exp. Eye Res.*, vol. 90, pp. 624–633, 2010.

[38] A. Eliasy *et al.*, "Determination of Corneal Biomechanical Behavior in-vivo for Healthy Eyes Using CorVis ST Tonometry: Stress-Strain Index," *Front. Bioeng. Biotechnol.*, vol. 7, p. 105, May 2019.

[39] R. W. Ogden, "Compressible Rubberlike Solids Large deformation isotropic elasticity : on the correlation of theory and experiment for compressible rubberlike solids," *Proc. R. Soc. A Math. Phys. Eng. Sci.*, vol. 328, no. 1575, pp. 567–583, 1972.

[40] R. W. Ogden, *Non-linear elastic deformations*. Dover Publications, 1997.

[41] A. Pandolfi and G. A. Holzapfel, "Three-Dimensional Modeling and Computational Analysis of the Human Cornea Considering Distributed Collagen Fibril Orientations," *J. Biomech. Eng.*, vol. 130, no. 6, p. 61006, Dec. 2008.

[42] Abaqus, "ABAQUS/Standard analysis user's manual v14.2," *SIMULIA*, 2014.

[43] G. J. (Gordon J. Van Wylen and R. E. Sonntag, *Fundamentals of classical thermodynamics*. Wiley, 1985.

[44] A. Villamarin, S. Roy, R. Hasballa, O. Vardoulis, P. Reymond, and N. Stergiopulos, "3D simulation of the aqueous flow in the human eye," *Med. Eng. Phys.*, vol. 34, no. 10, pp. 1462–1470, Dec. 2012.

[45] NASA, "Turbulence Modeling Resource: The Spalart-allmaras Turbulence," *Recherche*, 2011. [Online]. Available: https://turbmodels.larc.nasa.gov/.

[46] H. K. Versteeg and W. Malalasekera, "An Introduction to Computational Fluid Dynamics - The Finite Volume Method," *Fluid flow handbook. McGraw-Hill …*. 1995.

[47] E. E. Shpilrain, “AIR (PROPERTIES OF),” *A-to-Z Guid. to Thermodyn. Heat Mass Transf. Fluids Eng.*, vol. a, 2006.

[48] P. J. Rigden, “Viscosity of air [15],” *Nature*, vol. 141, no. 3558. p. 82, 1938.

[49] A. A. Joda, M. M. S. Shervin, D. Kook, and A. Elsheikh, “Development and validation of a correction equation for Corvis tonometry,” *Comput. Methods Biomech. Biomed. Engin.*, vol. 19, no. 9, pp. 943–953, 2015.

[50] D. Shirokoff and R. R. Rosales, “An efficient method for the incompressible Navier-Stokes equations on irregular domains with no-slip boundary conditions, high order up to the boundary,” 2010.

[51] C. T. Kelley, “Iterative Methods for Linear and Nonlinear Equations,” *Society*, vol. 16, no. 11, p. 166, 1995.

[52] J. Drkošová, A. Greenbaum, M. Rozložník, and Z. Strakoš, “Numerical stability of GMRES,” *BIT Numer. Math.*, vol. 35, no. 3, pp. 309–330, 1995.

[53] A. Pueyo and D. W. Zingg, “Efficient Newton-Krylov Solver for Aerodynamic Computations,” *AIAA J.*, 1998.

[54] G. W. Su, J. T. Geller, J. R. Hunt, and K. Pruess, “_A review of algebraic multigrid.pdf,” *Vadose Zo. J*, vol. 3, no. 2, pp. 592–601, 2004.

[55] D. R. Kincaid, J. R. Respess, D. M. Young, and R. R. Grimes, “Algorithm 586: ITPACK 2C: A FORTRAN Package for Solving Large Sparse Linear Systems by Adaptive Accelerated Iterative Methods,” *ACM Trans. Math. Softw.*, vol. 8, no. 3, pp. 302–322, 1982.

[56] J. Crank and P. Nicolson, “A practical method for numerical evaluation of solutions of partial differential equations of the heat-conduction type,” *Math. Proc. Cambridge Philos. Soc.*, vol. 43, no. 1, pp. 50–67, 1947.

[57] R. Courant, H. Lewy, and K. Friedrichs, “Über die partiellen Differenzengleichungen der mathematischen Physik,” *Math. Ann.*, vol. 100, pp. 32–74, 1928.

[58] C. A. de Moura and C. S. Kubrusly, Eds., *The Courant–Friedrichs–Lewy (CFL) Condition*. Boston: Birkhäuser Boston, 2013.

[59] C. B. Laney, *Computational Gasdynamics*. Cambridge: Cambridge University Press, 1998.

[60] M. Kcharik, R. Liska, P. Váchal, and M. Shashkov, “Arbitrary Lagrangian-Eulerian (ALE) Method in compressible fluid dynamics,” *Appl. Math. Sci.*, pp. 1–6, 2007.

[61] J. Hron and S. Turek, “A Monolithic FEM/Multigrid Solver for an ALE Formulation of Fluid-Structure Interaction with Applications in Biomechanics,” in *Fluid-Structure Interaction*, Berlin, Heidelberg: Springer Berlin Heidelberg, 2006, pp. 146–170.

[62] J. Donea, A. Huerta, J.-P. Ponthot, and A. Rodríguez-Ferran, “Arbitrary Lagrangian-Eulerian Methods,” in *Encyclopedia of Computational Mechanics Second Edition*, 2017, pp. 1–23.

[63] M. Souli and J. P. Zolesio, “Arbitrary Lagrangian-Eulerian and free surface methods in fluid mechanics,” *Comput. Methods Appl. Mech. Eng.*, vol. 191, no. 3–5, pp. 451–466, 2001.

[64] O. F. Villavicencio, F. Gilani, M. A. Henriquez, L. Izquierdo, and R. R. Ambrósio, “Independent Population Validation of the belin / Ambrósio Enhanced Ectasia display : Implications for Keratoconus studies and screening.” .

[65] W. J. Dupps and S. E. Wilson, “Biomechanics and wound healing in the cornea,” *Experimental Eye Research*, vol. 83, no. 4. pp. 709–720, 2006.

[66] A. Pandolfi, G. Fotia, and F. Manganiello, “Finite element simulations of laser refractive corneal surgery,” in *Engineering with Computers*, 2009, vol. 25, no. 1, pp. 15–24.

[67] A. Gefen, R. Shalom, D. Elad, and Y. Mandel, “Biomechanical analysis of the keratoconic cornea,” *J. Mech. Behav. Biomed. Mater.*, vol. 2, no. 3, pp. 224–236, 2009.

[68] A. Sinha Roy, M. Kurian, H. Matalia, and R. Shetty, “Air-puff associated quantification of non-linear biomechanical properties of the human cornea in vivo,” *J. Mech. Behav. Biomed. Mater.*, vol. 48, no. July, pp. 173–182, 2015.

Tables

Table 1: Clinical dataset used in validation of the numerical model of the air puff test

Datasets	Patients	Age (years)	CCT (μm)	CVS-IOP (mmHg)
Dataset 1 (Milan)	225	38 ± 17.2 (7–91)	543 ± 31.5 (458–635)	15.7 ± 2.35 (11–25)
Dataset 2 (Rio)	251	43 ± 16.5 (8–87)	539 ± 33.2 (454–629)	14.8 ± 3.06 (6–34)

*Note: CCT is central corneal thickness; CVS-IOP is CorVis IOP measurement

Table 2: Descriptive statistics of 110 models of the parametric study, the bold line separates input from output parameters

Variable	Mean	Std. Deviation	Minimum	Maximum
IOP (mmHg)	18.36	6.25	10	25

CCT (µm)	550.45	73.99	445	645
µ	0.0712	0.0236	0.0422	0.1082
R (mm)	7.82	0.33	7.4	8.4
A1 Time (ms)	9.66	0.97	7.81	12.47
A1 Length (mm)	2.15	0.19	1.91	2.62
A1 Velocity (mm/s)	0.13	0.04	0.06	0.21
HC Time (ms)	16.21	0.36	15.3	16.9
Peak Distance (mm)	4.58	0.95	2.46	6.62
A1 Def. Amp.(mm)	0.23	0.05	0.17	0.39
HC Def. Amp.(mm)	0.84	0.3	0.42	1.77
AP1(mmHg)	42.09	12.09	18.82	75.24
SP-HC	34.69	21.92	5	109.59

Table 3: Correlation and relationship significance analysis between input and output parameters of the parametric study

Variable		A1 Time(ms)	A1 Length(mm)	A1 Velocity(mm/s)	HC Time(ms)	Peak Dist.(mm)	A1 Deformation Amp.(mm)	HC Deformation Amp.(mm)	AP1 (mmHg)	SP-HC Stiffness parameter
IOP [mmHg]	Pearson Correlation (r)	.725**	-.455**	-.731**	-.255**	-.616**	-.403**	-.635**	.736**	.442**
	Sig. (2-tailed)	0.000	0.000	0.000	0.007	0.000	0.000	0.000	0.000	0.000
CCT [µm]	Pearson Correlation (r)	.382**	.637**	-.206*	-0.122	-.500**	.673**	-.493**	.385**	.468**
	Sig. (2-tailed)	0.000	0.000	0.031	0.204	0.000	0.000	0.000	0.000	0.000
µ	Pearson Correlation (r)	.338**	.471**	-.367**	-.280**	-.407**	.432**	-.377**	.355**	.434**
	Sig. (2-tailed)	0.000	0.000	0.000	0.003	0.000	0.000	0.000	0.000	0.000
R [mm]	Pearson Correlation (r)	-0.007	-0.056	-0.067	0.032	0.088	-.253**	-0.052	0.007	-0.088
	Sig. (2-tailed)	0.946	0.564	0.486	0.741	0.362	0.008	0.592	0.945	0.362

*Note: IOP is intraocular pressure; CCT is central corneal thickness; µ is corneal material stiffness coefficient; R is corneal curvature radius; A1 is the first applanation; HC is the highest concavity; AP1 is the first applanation pressure; SP-HC is the stiffness parameter at highest concavity

Preprints (www.preprints.org) | NOT PEER-REVIEWED | Posted: 25 September 2019 doi:10.20944/preprints201909.0278.v1

Peer-reviewed version available at *Int. J. Environ. Res. Public Health* **2019**, *17*, 54; doi:10.3390/ijerph17010054

Figures

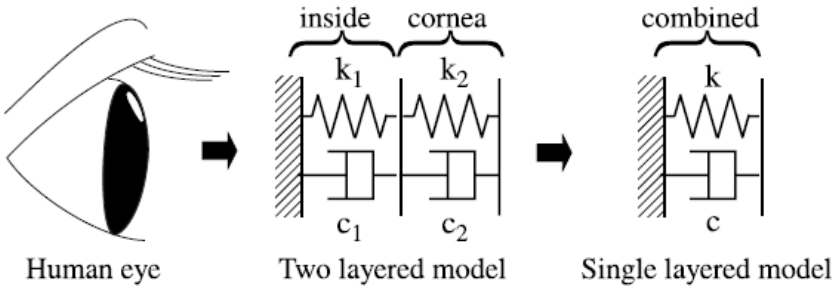

Figure 1: Dynamic model of the human eye as one and two degrees of freedom [14]

(a)

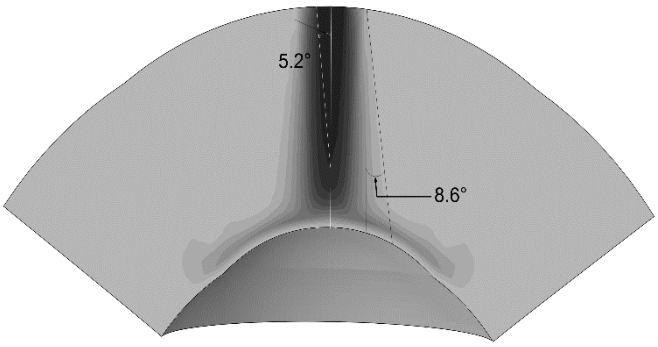

(b)

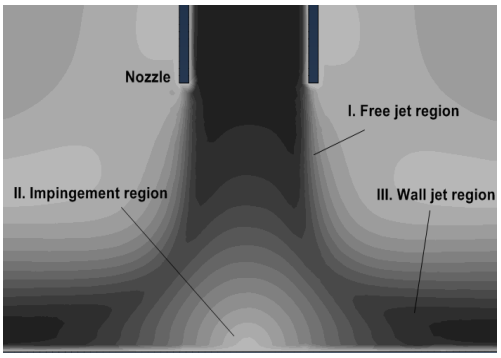

Figure 2: Round impinging jet diffusion (a), the impinging jet different regions (b)

Preprints (www.preprints.org) | NOT PEER-REVIEWED | Posted: 25 September 2019 doi:10.20944/preprints201909.0278.v1

Peer-reviewed version available at Int. J. Environ. Res. Public Health 2019, 17, 54; doi:10.3390/ijerph17010054

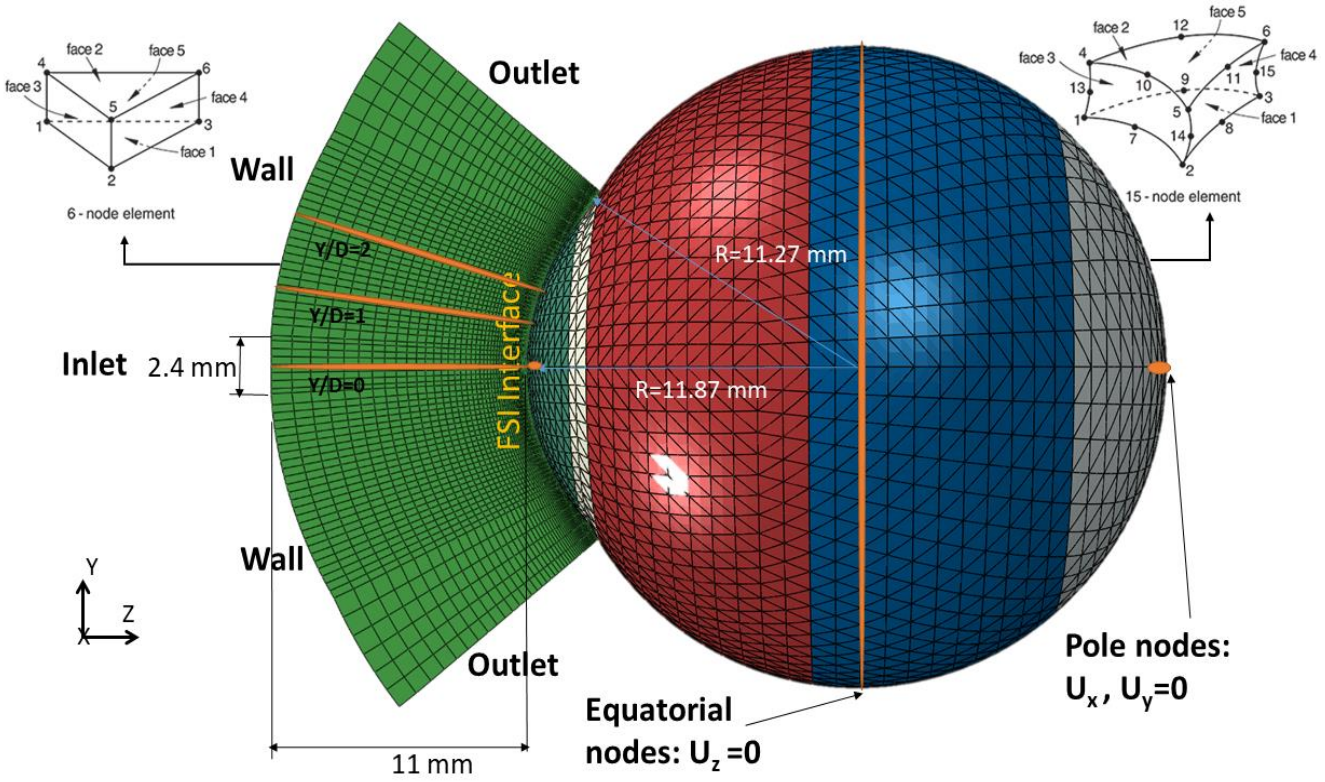

Figure 3: Geometry definition of the air puff and eye domains showing key dimensions, element types and boundary conditions. Ux , Uy , Uz are the deformations in the three dimensions

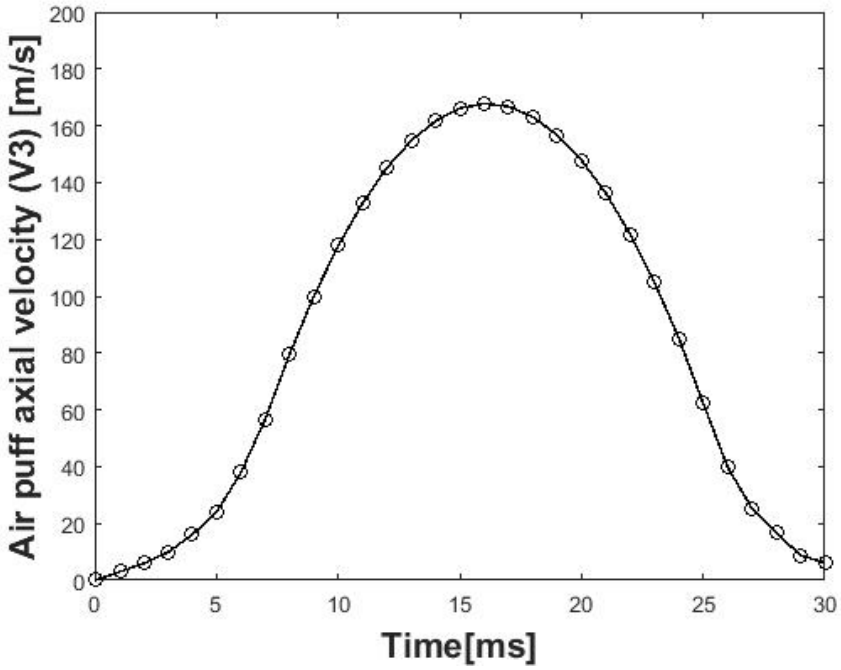

Figure 4: Temporal velocity profile at the puff nozzle fed as inlet boundary condition to CFD air puff model

Preprints (www.preprints.org) | NOT PEER-REVIEWED | Posted: 25 September 2019 doi:10.20944/preprints201909.0278.v1

Peer-reviewed version available at Int. J. Environ. Res. Public Health 2019, 17, 54; doi:10.3390/ijerph17010054

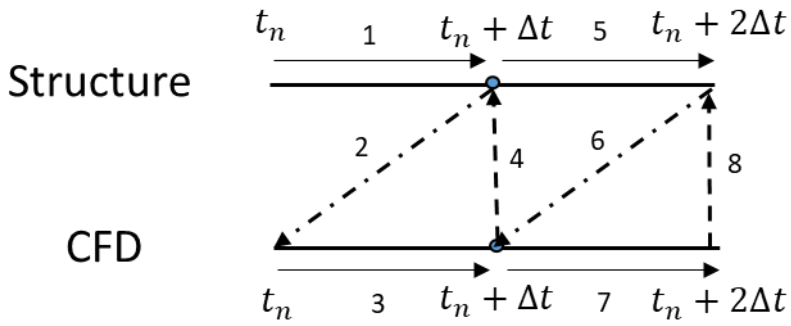

Figure 5: Flow of the solution in the fluid structure interaction coupling at each time step

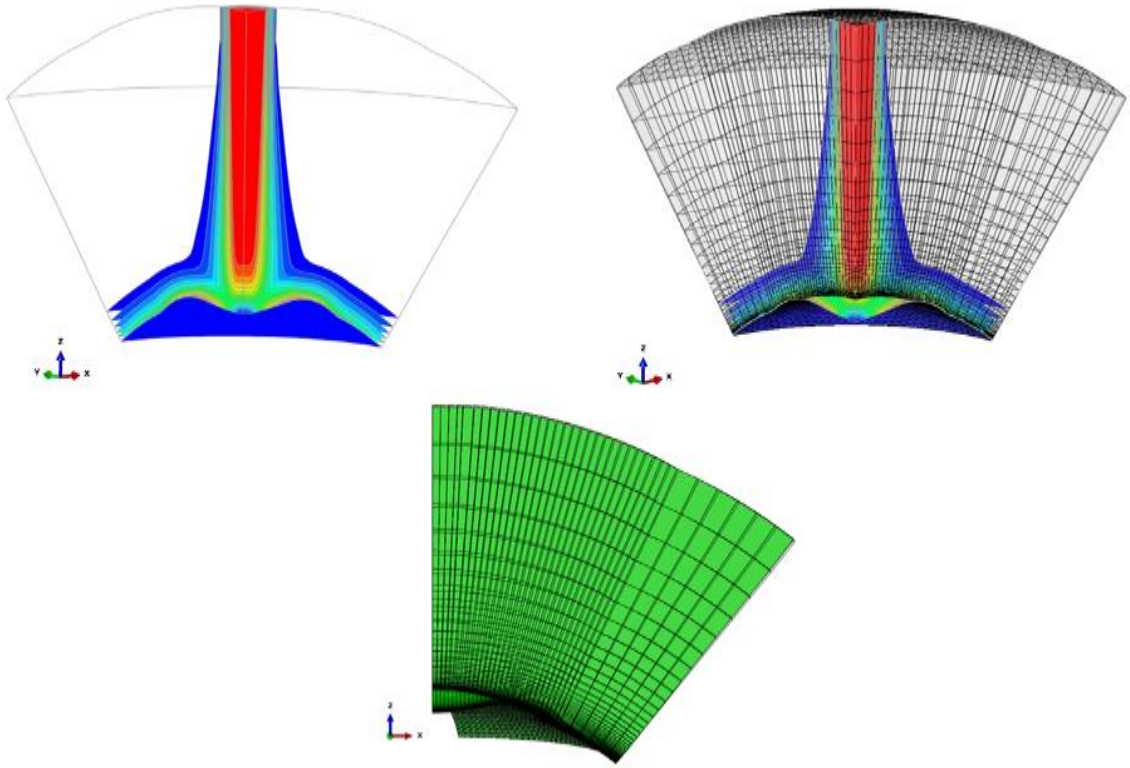

Figure 6: Arbitrary Lagrangian-Eulerian (ALE) deforming mesh shown on a quarter model of the air puff

Preprints (www.preprints.org) | NOT PEER-REVIEWED | Posted: 25 September 2019 doi:10.20944/preprints201909.0278.v1

Peer-reviewed version available at Int. J. Environ. Res. Public Health 2019, 17, 54; doi:10.3390/ijerph17010054

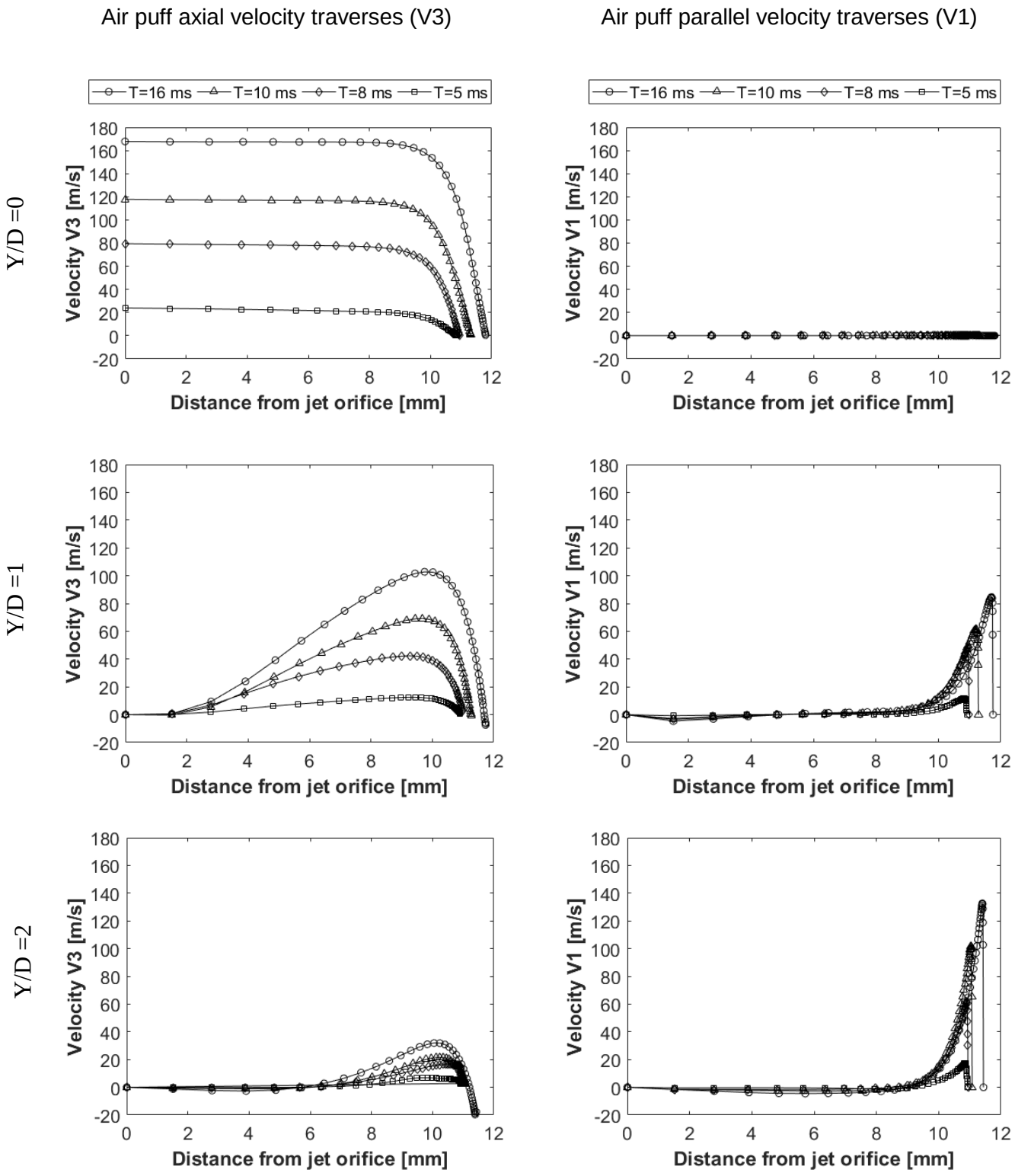

Figure 7: Air puff velocity components (V3 and V1) at axial traverses Y/D=0, Y/D=1, Y/D=2 and 4 time steps at T= 5, 8, 10, 16 ms

Preprints (www.preprints.org) | NOT PEER-REVIEWED | Posted: 25 September 2019 doi:10.20944/preprints201909.0278.v1

Peer-reviewed version available at Int. J. Environ. Res. Public Health 2019, 17, 54; doi:10.3390/ijerph17010054

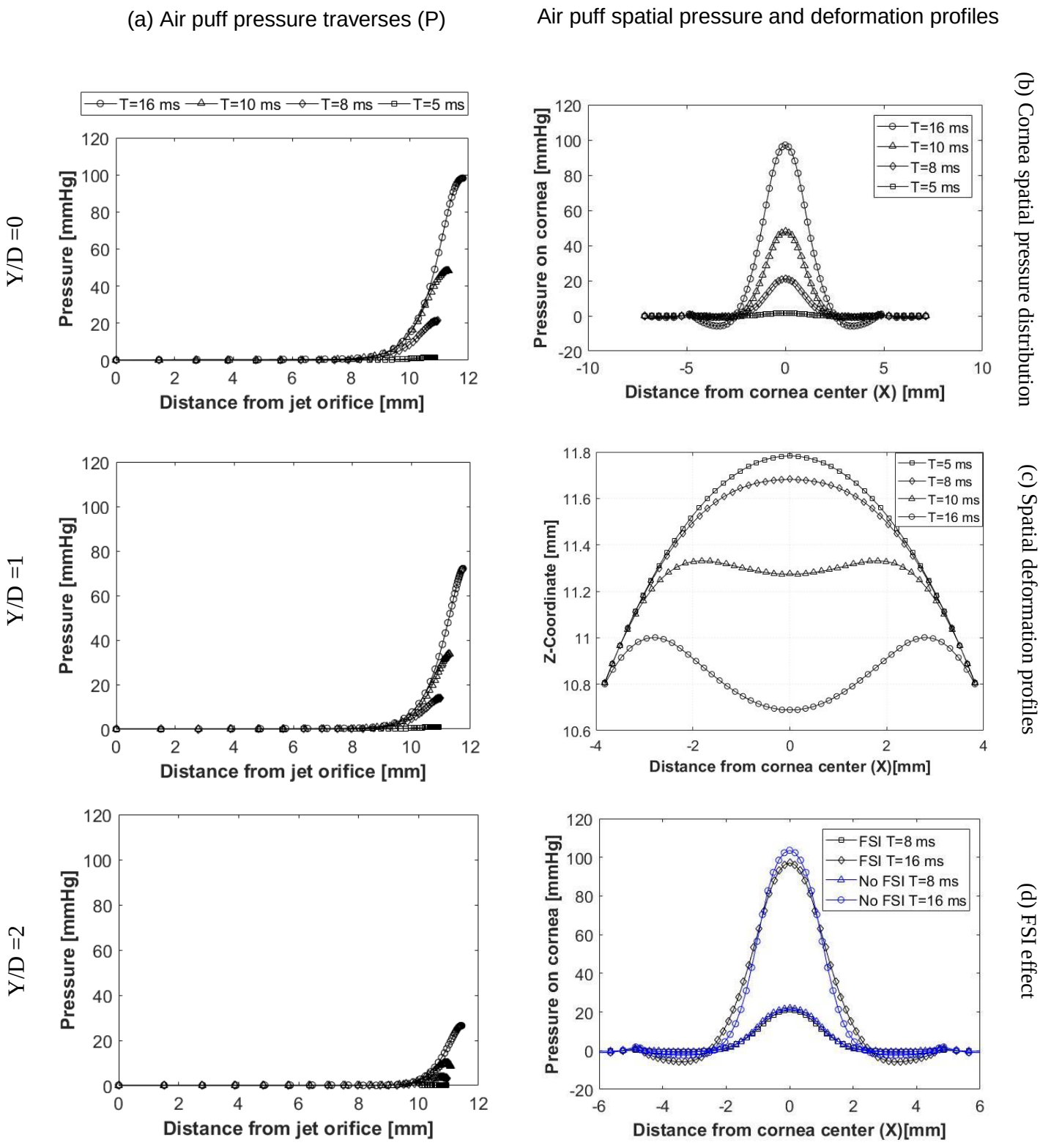

Figure 8: Air puff total pressure traverses (P), at Y/D=0, Y/D=1, Y/D=2 (a), spatial pressure distribution on the cornea (b), cornea deformation profiles (c) and explanation of the FSI effect on the pressure distribution (d)

Preprints (www.preprints.org) | NOT PEER-REVIEWED | Posted: 25 September 2019 doi:10.20944/preprints201909.0278.v1

Peer-reviewed version available at *Int. J. Environ. Res. Public Health* **2019**, *17*, 54; doi:10.3390/ijerph17010054

(a)

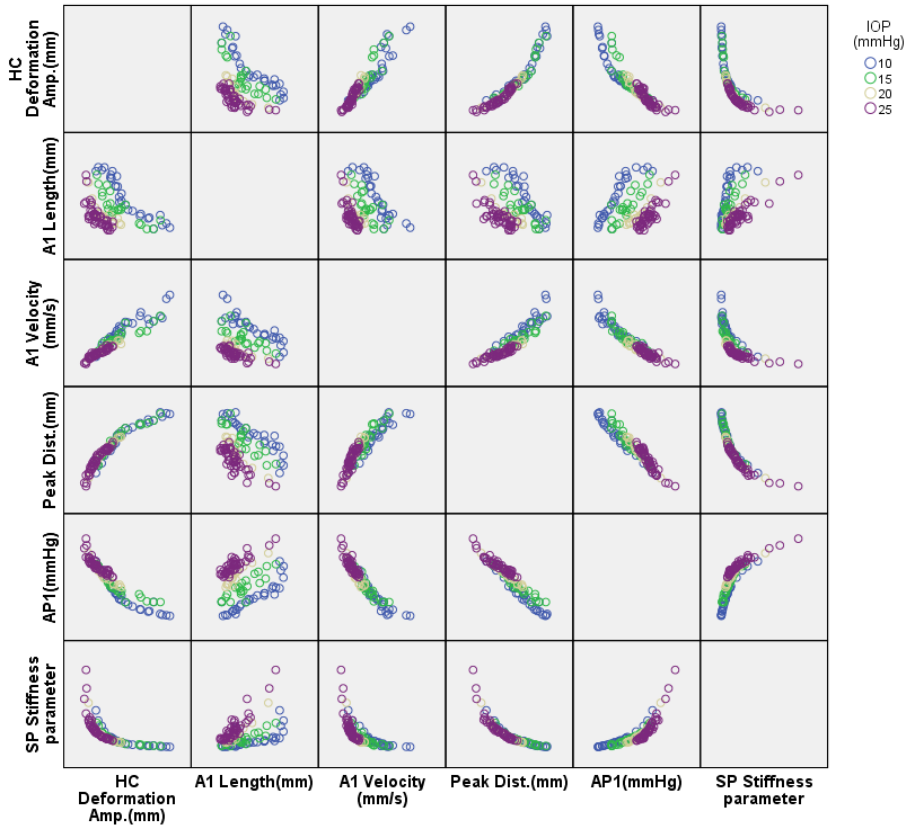

(c)

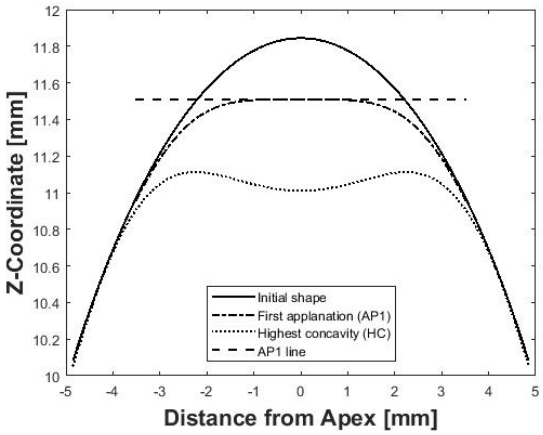

(b)

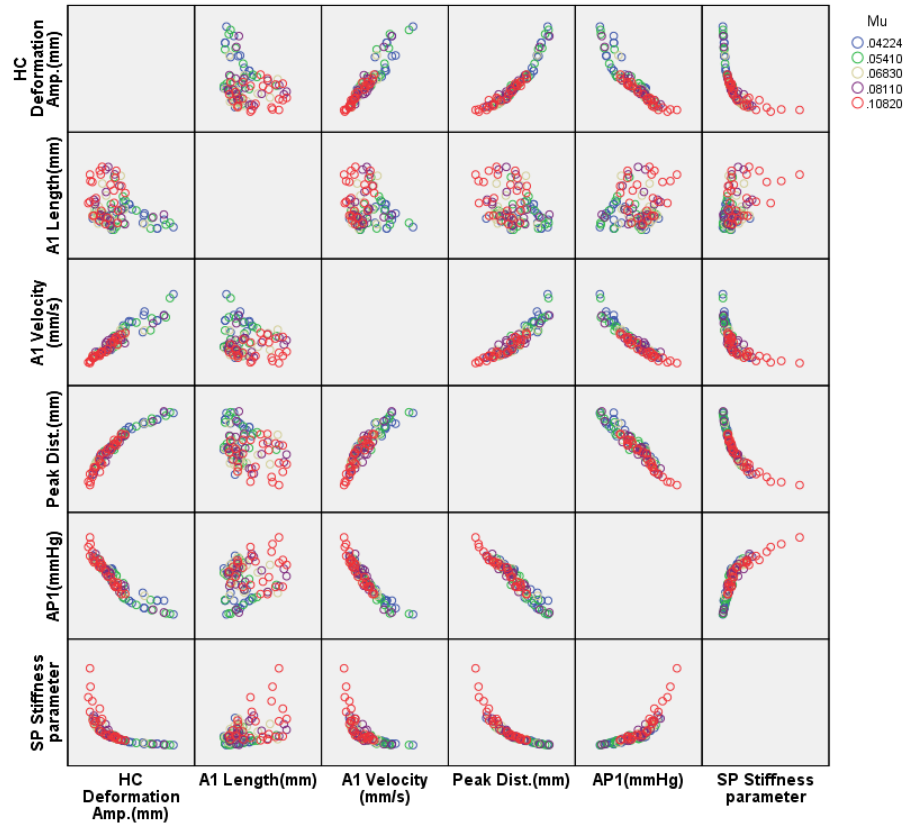

Figure 9: Influence matrix of changing intraocular pressure (IOP) (a) and corneal material stiffness (b) on corneal response parameters, while (c) illustrates the corneal profile stages

Preprints (www.preprints.org) | NOT PEER-REVIEWED | Posted: 25 September 2019 doi:10.20944/preprints201909.0278.v1

Peer-reviewed version available at *Int. J. Environ. Res. Public Health* **2019**, *17*, 54; doi:10.3390/ijerph17010054

Clinical case 1

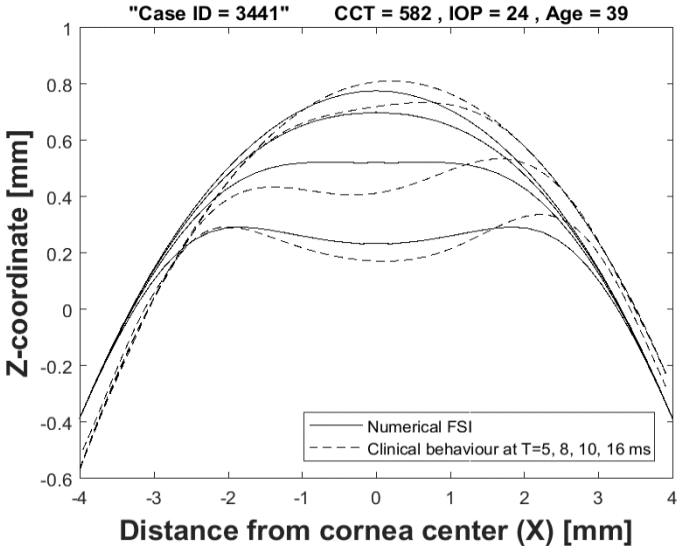

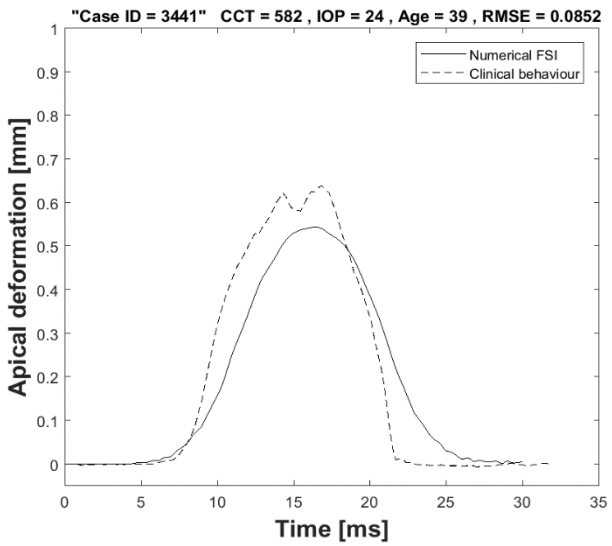

Clinical case 2

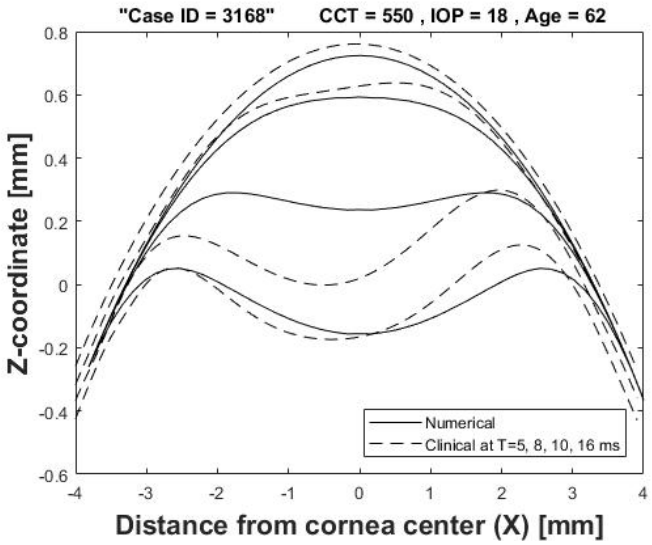

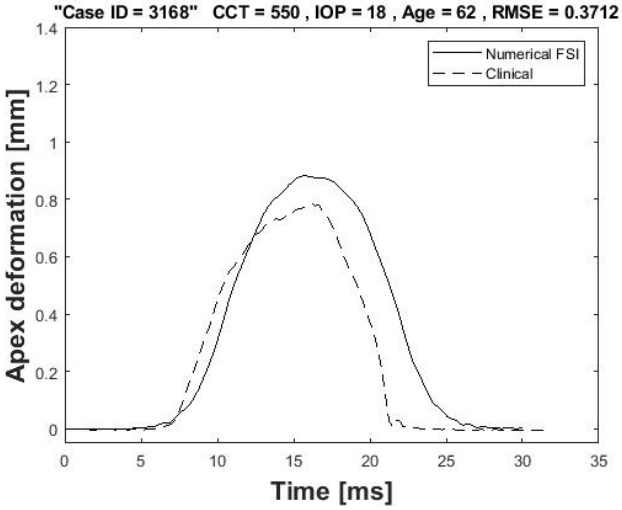

Clinical case 3

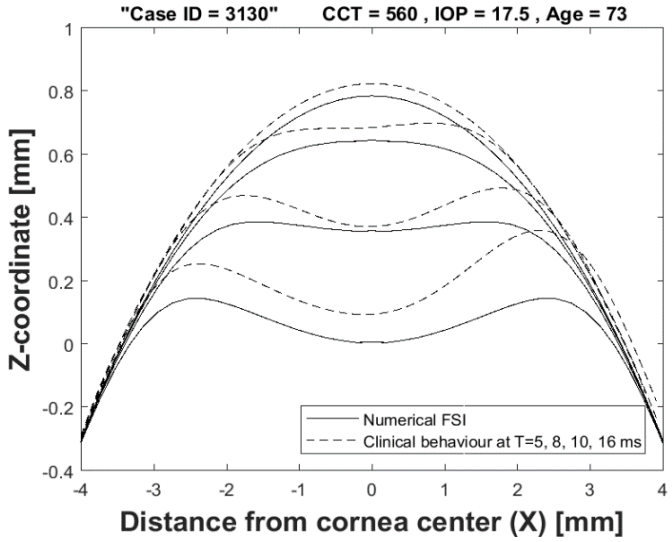

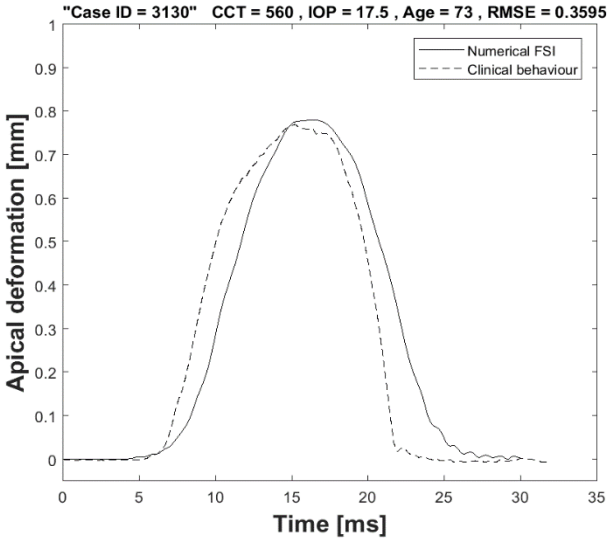

Figure 10: Spatial corneal deformation and temporal apical deformation comparison with 3 clinical cases

Preprints (www.preprints.org) | NOT PEER-REVIEWED | Posted: 25 September 2019 doi:10.20944/preprints201909.0278.v1

Peer-reviewed version available at Int. J. Environ. Res. Public Health 2019, 17, 54; doi:10.3390/ijerph17010054

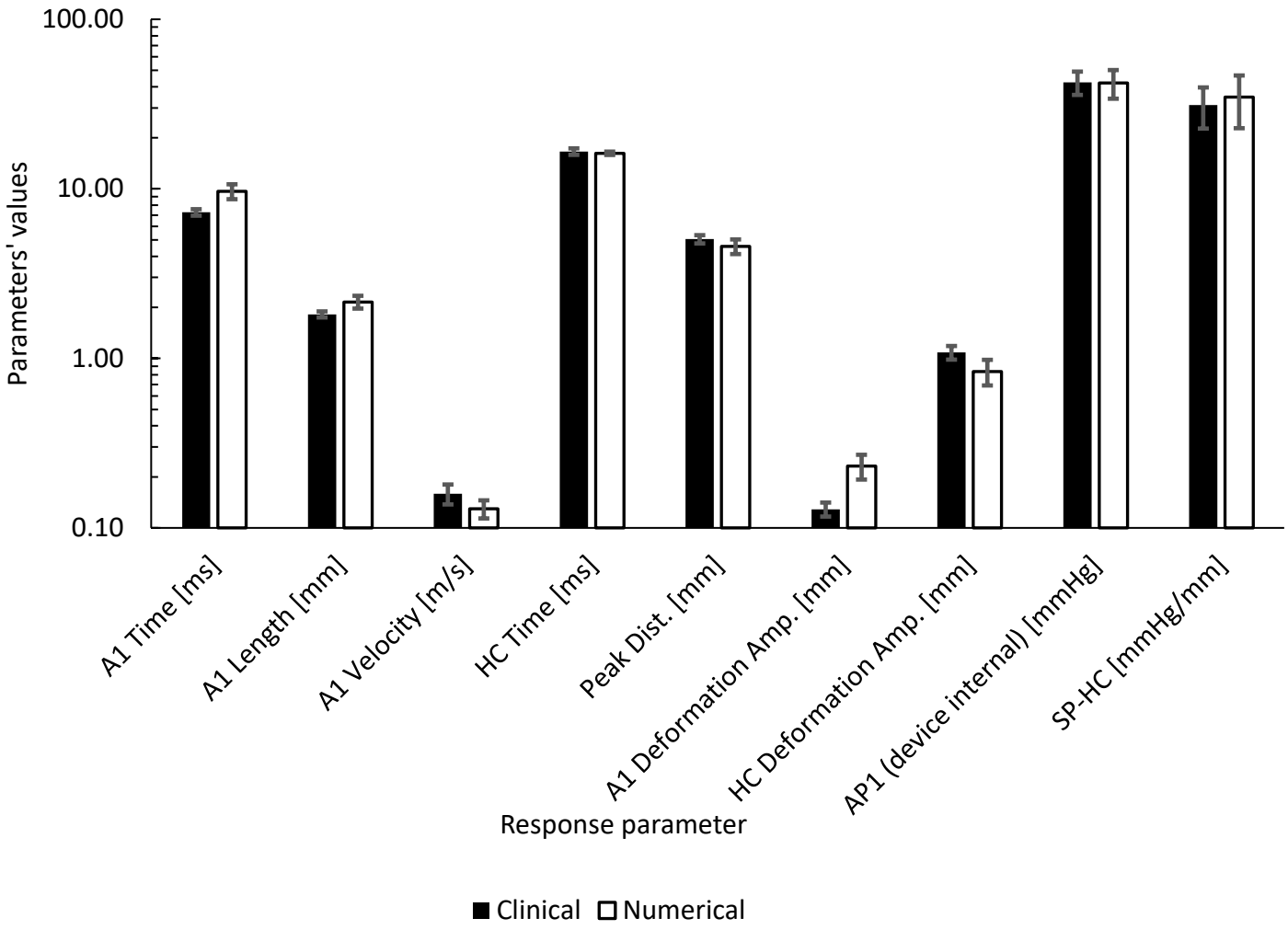

Figure 11: Corneal response parameters' comparison between clinical and numerical results of the parametric study